



Selective oxidation of methanol to dimethoxymethane on V_2O_5 – MoO_3 – γ - Al_2O_3 catalysts

Yali Meng^{a,b}, Tuo Wang^{a,b}, Shuang Chen^{a,b}, Yujun Zhao^{a,b},
Xinbin Ma^{a,b}, Jinlong Gong^{a,b,*}

^a Key Laboratory for Green Chemical Technology of Ministry of Education, School of Chemical Engineering and Technology, Tianjin University, Tianjin 300072, China

^b Collaborative Innovation Center of Chemical Science and Engineering, Tianjin 300072, China



ARTICLE INFO

Article history:

Received 30 January 2014

Received in revised form 3 May 2014

Accepted 5 May 2014

Available online 14 May 2014

Keywords:

Methanol

Dimethoxymethane

V_2O_5 – MoO_3 – γ - Al_2O_3 catalysts

Redox cycle

Brønsted acid sites

ABSTRACT

This paper describes the design and application of V_2O_5 – MoO_3 – γ - Al_2O_3 catalysts for the selective oxidation of methanol to dimethoxymethane (DMM). The V_2O_5 – MoO_3 – γ - Al_2O_3 catalysts exhibit superior performance for DMM yield than the corresponding samples with V and Mo species only, even at relatively low temperatures. The origin of high DMM yield of the V_2O_5 – MoO_3 – γ - Al_2O_3 catalysts is explored and attributed to the synergistic effect of V and Mo mixed oxides presented on the surface of the catalyst. The synergism can be ascribed to (i) the completion of a redox cycle and (ii) the enrichment of weak Brønsted acidic sites. The redox cycle of V–O–Mo oxides could be completed through electron transfer between lattice oxygen and metal cations. The V species exhibits a superior performance in the adsorption and activation of gaseous oxygen, as well as enhanced capability to restore the lattice oxygen and suppress the aggregation of Mo species. The enrichment of weak Brønsted acidic sites is attributed to the addition of MoO_3 and the increase of partially reduced V and Mo species, respectively, which is critical to increasing the DMM yield. By adjusting the content of V_2O_5 and MoO_3 , we have obtained a 14 V_2O_5 –14 MoO_3 – γ - Al_2O_3 catalyst with the optimized amounts of redox sites and acidic sites, which exhibits a 54% methanol conversion with a DMM selectivity of 92% at 393 K.

© 2014 Elsevier B.V. All rights reserved.

1. Introduction

Dimethoxymethane (DMM) has various industrial applications; particularly, it has been used as a potential proctane with a high chemical stability, high cetane number and high oxygen content [1]. It is also an important intermediate in organic synthesis, and has been utilized as an excellent solvent in perfume and pharmaceutical industries [2]. Commercially, DMM is produced through acetalization of methanol and formaldehyde, which, however, suffers from high reaction temperature, complicated procedures, and severe equipment corrosion [3]. Alternatively, one-step selective oxidation of methanol to DMM could potentially circumvent these problems, and hence has attracted much attention.

Direct selective oxidation of methanol to DMM typically involves two steps: methanol oxidation to formaldehyde on redox

sites and subsequent acetalization reactions of formaldehyde with another methanol molecules forming DMM on acidic sites [4]. In order to attain high DMM yield, appropriately balanced redox ability and acidity of the catalyst are required. Excessive redox sites and insufficient acidic sites lead to the production of methyl formate (MF) and oxycarbide. Excessive acidic sites would generate a large number of dimethyl ether (DME).

Fundamental research on the development of this process has been primarily focused on the catalysts design and understanding reaction mechanisms. Several catalytic systems have been reported to be active for the methanol oxidation to DMM, including supported Re oxide and Re-based mixed oxides (60–98% DMM selectivity and 60.3–15.4% methanol conversion at 300–513 K with a methanol content of 4.8–7.4 vol% [5–12]), variations of V/TiO₂-based catalysts (89–92% DMM selectivity and 41–60% methanol conversion at 393 K with a methanol content of 5 vol% [13–18]), modified V/TS-1 formulations [19], amorphous multi-metal samples [3,20], bulk or supported heteropoly acids catalysts (30–67% DMM selectivity and 20.3–68.4% methanol conversion at 453–513 K with a methanol content of 9.2 vol%) [2,9,21–23], and FeMo formulations (89.7% DMM selectivity and 56.7% methanol

* Corresponding author at: Tianjin University, School of Chemical Engineering and Technology, 92 Weijin Road, Nankai District, Tianjin 300072, China.
Tel.: +86 22 87401818; fax: +86 22 87401818.

E-mail address: jlgong@tju.edu.cn (J. Gong).

conversion with a methanol content of 20 vol% and 4.6 kg DMM h⁻¹ kg cat⁻¹ at 553 K [24–26]. It has been shown that amorphous Mo₁₂V₃W_{1.2}Cu_{1.2}SB_{0.5}O_x [20] has an optimal performance with 90% DMM selectivity at methanol conversion of 68% (a methanol content of 5 vol%) at 553 K with a gas hourly space velocity (GHSV) of 22,000 mL g⁻¹ h⁻¹.

MoO₃/Al₂O₃-based catalysts have been used in a series of reactions such as hydrodesulfurization (HDS) [27], oxidative dehydrogenation (ODS) [28–31], and partial oxidation of hydrocarbons and alcohols (ODH) [32–34]. However, they typically suffer from low reaction rates due to high absorption energies in the ODH process [35]. Chen et al. has reported that the activation energy of the alkane C–H bond depends on the ability of the active oxide domains to transfer electrons from lattice oxygen to metal cations [36]. When molybdenum based catalysts are doped with promoters, high reaction rates could be obtained. For example, Fe–Mo catalysts have been industrially used for the selective oxidation of methanol to formaldehyde (FA). In addition to the rivet and electron transfer role of Fe, Mo is the active site for the cleavage of the C–H bond and production of formaldehyde [37–39]. As vanadium-based catalyst has superior redox capabilities at low temperatures in oxidation processes [17,19,35], we introduce vanadium species to MoO₃/Al₂O₃ catalysts to attain stronger redox ability. Indeed, V₂O₅–MoO₃-based catalysts have been applied in selective oxidation of hydrocarbon compounds; the excellent oxidation performance was owing to the remarkable redox ability of V and Mo mixed oxides [40–42].

This paper describes the design, characterization, and application of V₂O₅–MoO₃/Al₂O₃ catalysts in methanol oxidation to DMM based on the tunable redox property of vanadium and molybdenum oxides and the notable acidic property of aluminum oxide. The redox ability could be controlled by the availability of V and Mo oxides, with the acidity provided by the Al₂O₃ support. V₂O₅/Al₂O₃ and MoO₃/Al₂O₃ samples have also been prepared for reference. The catalysts are characterized by N₂ adsorption/desorption, X-ray diffraction (XRD), Fourier transform infrared spectroscopy (FTIR), methanol pulse chemisorption, Raman spectroscopy, pyridine adsorption of FTIR spectroscopy, temperature programed desorption of ammonia (NH₃-TPD), temperature programed reduction (H₂-TPR), temperature programed reduction–temperature programed oxidation (TPR-TPO), temperature programed desorption of oxygen (O₂-TPD) and X-ray photoelectron spectroscopy (XPS). The catalytic activities and redox and acidic behaviors of V₂O₅–MoO₃/Al₂O₃ catalysts are also analyzed. Compared with the reference samples, the synergism of V and Mo species has been investigated.

2. Experimental

2.1. Catalyst preparation

A series of V₂O₅–MoO₃/Al₂O₃ catalysts with different V/Mo ratios were prepared by a wetness impregnation method. The MoO₃/Al₂O₃ and V₂O₅/Al₂O₃ catalysts were also prepared by the same method for comparison purpose. A γ -Al₂O₃ powder support (Jianzhong Co, surface area of 227 m² g⁻¹ and pore volume of 0.34 cm³ g⁻¹) was calcined in air at 573 K for 2 h prior to catalyst preparation. For the V₂O₅/Al₂O₃ catalyst, the required amount of ammonium metavanadate was dissolved in an oxalic acid aqueous solution (2 M) and mixed with the support in continuous stirring. In the case of MoO₃/Al₂O₃, an aqueous solution containing the desired amount of ammonium heptamolybdate was mixed with the support. The V₂O₅–MoO₃/Al₂O₃ catalysts were obtained by successive impregnation of calcined MoO₃/Al₂O₃ samples with an ammonium metavanadate solution. Subsequently, final catalyst samples were

obtained upon the evaporation of the solvent at 353 K, and then dried at 393 K for 12 h and calcined at 773 K for 6 h in furnace. The catalyst samples were named as xV₂O₅/Al₂O₃, yMoO₃/Al₂O₃, and xV₂O₅–yMoO₃/Al₂O₃, where x, y represents the mass concentration of V₂O₅ and MoO₃ in the catalysts, respectively.

2.2. Catalyst characterization

XRD patterns were collected on a Rigaku D/Max-2500 diffractometer using C-filtered Cu K α radiation ($\lambda = 1.54056$ Å), operated at 40 kV and 200 mA, at a scan rate of 0.02° s⁻¹ from 10 to 90°.

FTIR spectra were recorded on a Thermo Scientific Nicolet 6700 FTIR spectrometer with a deuterated triglycine sulphate (DTGS) detector. The spectra were obtained in the 4000–400 cm⁻¹ range with a resolution of 4 cm⁻¹ and 128 scans. In each experiment, a self-supporting wafer (18 mm dia.) made of 2 mg sample were mixed with 198 mg KBr. The samples were pretreated in a vacuum drier at 393 K for 4 h before any measurements.

FTIR spectra of pyridine absorption were recorded using the same FTIR spectrometer in the range of 4000–450 cm⁻¹ (32 scans, 4 cm⁻¹). All samples were evacuated at approximately 10⁻⁴ Pa and heated at 573 K for 30 min, and then saturated by pyridine at 393 K for 30 min; samples were evacuated to eliminate the physically adsorbed pyridine for 30 min. All scans were acquired at 393 K.

Raman spectra were collected using a Thermo Scientific DXRTM Raman Microscope with a green semiconductor laser (532 nm) as the excitation source. Samples were pretreated in a vacuum drier at 393 K for 12 h before any measurements. Raman spectra were recorded at ambient temperature.

N₂ adsorption/desorption analysis was performed at 77 K using a Micromeritics Tristar 300 surface area and porosity analyzer. The specific surface area was determined by the Bruaer–Emmett–Teller (BET) method. The pore parameters (pore volume and pore diameter) were evaluated from the desorption branch of isotherms based on the Barrett–Joyner–Halenda (BJH) model.

NH₃-TPD and O₂-TPD spectra and methanol pulse chemisorption were recorded on a Micromeritics Autochem 2920 chemisorption analyzer. The catalyst (150 mg) was pretreated at 573 K under Ar flow (30 mL min⁻¹) for 1 h, and was then cooled down to 333 K. NH₃ (or 10 vol% O₂) was subsequently introduced into the flow system for 30 min. The TPD spectra was recorded at a ramp rate of 10 K min⁻¹ from 333 K to 973 K (1050 K) under a He flow. H₂-TPR measurements were carried out on a 2910 chemisorption instrument with a thermal conductivity detector (TCD). The sample (150 mg) was pretreated at 573 K under Ar flow (30 mL min⁻¹) for 1 h, and cooled to 333 K. The sample was then contacted with a H₂:Ar mixture (10 vol% H₂) at a flow rate of 40 mL min⁻¹ and heated at a rate of 10 K min⁻¹ from room temperature to 1100 K. The signal of methanol pulse chemisorption is recorded at a temperature of 373 K in CH₃OH:He mixture flow (35 vol% methanol) until at least three successive peaks show the same area.

Thermal programed reduction (TPR) and thermal-programed re-oxidation (TPO) tests were carried out using the same Autochem 2920 chemisorption analyzer (Micromeritics). The reducing and oxidizing gases were composed of 10% (v/v) H₂ in Ar and 10% (v/v) O₂ in He, respectively. Each sample was heated in an Ar flow at 573 K for 1 h to eliminate weakly adsorbed water. After cooling to 373 K, Ar was replaced by the reducing gas (TPR measurement) and the linear temperature programed heating was started from room temperature to 923 K at 10 K min⁻¹, followed by a final isothermal step of 30 min at 923 K (a temperature selected based on H₂-TPR to avoid bulk reduction). The outlet gas from the reactor was analyzed with a TCD detector. After the reducing step, the catalysts were cooled and subjected to a re-oxidation treatment (TPO measurement), using the same heating procedure.

Table 1

Textural properties and catalytic activities of catalysts in the methanol oxidation reaction.

Sample	S_{BET} ($\text{m}^2 \text{g}^{-1}$)	Pore volume ($\text{cm}^3 \text{g}^{-1}$)	Pore size (nm)	Methanol conversion (%)	Selectivity (%)					Carbon balance (%)
					DMM	DME	MF	FA	CO_x	
$\gamma\text{-Al}_2\text{O}_3$	221	0.34	6.0	6.7	0.0	100	0.0	0.0	0.0	100
4 $\text{V}_2\text{O}_5/\text{Al}_2\text{O}_3$	175	0.34	5.8	13.2	47.4	34.3	18.3	0.0	0.0	100
8 $\text{V}_2\text{O}_5/\text{Al}_2\text{O}_3$	163	0.32	5.6	14.6	54.5	22.2	22.2	0.1	0.0	99.4
14 $\text{V}_2\text{O}_5/\text{Al}_2\text{O}_3$	160	0.30	5.6	34.6	65.5	17.3	16.4	0.8	0.0	99.0
20 $\text{V}_2\text{O}_5/\text{Al}_2\text{O}_3$	112	0.22	5.8	36.7	71.9	15.5	12.4	1.2	0.0	98.7
24 $\text{V}_2\text{O}_5/\text{Al}_2\text{O}_3$	121	0.26	6.8	33.7	74.8	12.3	9.4	2.5	0.9	98.6
4 $\text{MoO}_3/\text{Al}_2\text{O}_3$	213	0.35	5.8	8.2	33.4	14.5	52.1	0.0	0.0	99.8
8 $\text{MoO}_3/\text{Al}_2\text{O}_3$	200	0.30	6.0	11.8	40.4	37.2	22.4	0.0	0.0	99.9
14 $\text{MoO}_3/\text{Al}_2\text{O}_3$	182	0.27	6.0	28.2	76.7	9.4	13.3	0.6	0.0	99.5
20 $\text{MoO}_3/\text{Al}_2\text{O}_3$	142	0.23	6.3	30.2	84.6	13.2	2.2	0.0	0.0	99.7
24 $\text{MoO}_3/\text{Al}_2\text{O}_3$	130	0.25	5.8	26.2	86.6	11.2	1.3	0.7	0.2	99.4
14 $\text{V}_2\text{O}_5\text{-}8\text{MoO}_3/\text{Al}_2\text{O}_3$	130	0.24	6.1	33.1	72.3	12.3	15.3	0.1	0.0	100
14 $\text{V}_2\text{O}_5\text{-}11\text{MoO}_3/\text{Al}_2\text{O}_3$	113	0.22	5.8	46.4	91.0	5.8	3.2	0.0	0.0	99.3
14 $\text{V}_2\text{O}_5\text{-}14\text{MoO}_3/\text{Al}_2\text{O}_3$	98	0.17	5.9	54.2	92.1	5.6	2.3	0.0	0.0	100
14 $\text{V}_2\text{O}_5\text{-}20\text{MoO}_3/\text{Al}_2\text{O}_3$	85	0.17	6.7	49.3	88.4	8.1	2.8	0.7	0.0	99.4

The reaction temperature was 393 K; feed gas $\text{CH}_3\text{OH}/\text{O}_2/\text{N}_2 = 1/3/15$ vol; GHSV = 4000 h^{-1} ; reaction duration = 8 h.

XPS measurements were performed on a Physical Electronics PHI-1600 XPS system equipped with a hemispherical electron analyzer and an Mg $\text{K}\alpha$ X-ray source (1253.6 eV). The samples were fresh catalysts vacuum-dried at 393 K for 4 h prior to any measurements. The energy region of the photoelectrons was scanned at a pass energy of 29.35 eV. The binding energies were referenced to the C1s signal at 284.6 eV. The data was processed using the PHI Multipack Program (Gaussian peak fitting).

2.3. Catalyst activity measurements

Catalyst tests were carried out at the atmospheric pressure in a fixed-bed micro-reactor made of quartz with an inner diameter of 7 mm. Methanol was introduced into the reaction zone by bubbling O_2/N_2 (99.99%) through a glass saturator filled with methanol (99.9%) at 278 K (the CH_3OH partial pressure is 5.4036 kPa) at a constant GHSV of 4000 h^{-1} (feed gas $\text{CH}_3\text{OH}/\text{O}_2/\text{N}_2 = 1/3/15$ vol). In each test, 0.6 g of tableted catalyst (40–60 mesh) were loaded. In this reaction condition, the external and internal diffusion effects were found to be negligible (Figs. S1 and S2 in Supporting information). Before the reaction test, the catalyst was pretreated with a 20 vol% O_2/N_2 mixture gas (30 mL min^{-1}) at 673 K for 1 h. After cooled to the reaction temperature, a mixture of methanol, N_2 and O_2 was introduced to the catalyst bed with a flow rate of 40 mL min^{-1} . The reaction temperature was ranged from 373 to 473 K. The products were analyzed by an online Barcode Guy SP-2100 gas chromatography (GC) using a Propack T column connected with a flame ionization detector (FID) detector and a TCD detector. The FID line allows one to analyze methanol, MF, FA, DME and DMM, while the TCD line can quantify carbon monoxide (CO) and carbon dioxide (CO_2). The gas lines were kept at 373 K to prevent condensation of the reactant and products. The carbon balance was $99.5 \pm 1\%$ for all GC measurements.

3. Results

3.1. Structural properties

Physical properties of the catalysts are presented in Table 1. With the increase of V_2O_5 and MoO_3 loadings, BET surface areas are gradually decreased from 213 to 85 $\text{m}^2 \text{g}^{-1}$, whereas the pore volume and the mean pore radius are not significantly affected by vanadium and molybdenum additions and are in the range 0.17–0.24 $\text{cm}^3 \text{g}^{-1}$ and 5.9–6.7 nm, respectively. It is apparent that the BET surface area of $\text{V}_2\text{O}_5/\text{Al}_2\text{O}_3$ catalyst is slightly lower than

$\text{MoO}_3/\text{Al}_2\text{O}_3$ sample with the same loading, consistent with previous report that vanadium species tends to have a stronger interaction with the Al_2O_3 support than molybdenum species [43].

XRD patterns of vanadium- and molybdenum-based catalysts are shown in Fig. 1. The $\gamma\text{-Al}_2\text{O}_3$ characteristic peaks appear at 45.8, 67 and 37.6° (JCPDS 10-425) (Fig. 1a). For $\text{MoO}_3/\text{Al}_2\text{O}_3$ catalysts, the 14 $\text{MoO}_3/\text{Al}_2\text{O}_3$ sample only exhibits the Mo_4O_{11} crystal phase (sharp peak at 29.2°). High Mo loadings lead to the appearance of the MoO_3 crystal (sharp peaks at 10.8, 22.7, 28.5°) (JCPDS 47-1081) and a trace amount of $\text{Al}_2(\text{MoO}_4)_3$ (sharp peaks at 23.2, 27°) (JCPDS 23-0764). In case of $\text{V}_2\text{O}_5/\text{Al}_2\text{O}_3$ catalysts, V_2O_5 crystallites (sharp peaks at 20–30°) (JCPDS 45-1074) are detected only for the 24 $\text{V}_2\text{O}_5/\text{Al}_2\text{O}_3$ sample accompanied with the AlVO_4 crystal phase (sharp peak at 31°) (JCPDS 39-276) (Fig. 1e). For the 14 $\text{V}_2\text{O}_5\text{-}x\text{MoO}_3/\text{Al}_2\text{O}_3$ samples, molybdenum and vanadium species are well dispersed (Fig. 1g and f) at low Mo loadings. 14 $\text{V}_2\text{O}_5\text{-}14\text{MoO}_3/\text{Al}_2\text{O}_3$ possesses a V_2MoO_8 crystal phase (sharp peaks at 22, 23, 28, 31, 34°) (JCPDS 18-0851) and traces of V_2O_5 and MoO_3 crystal phases (Fig. 1h) [19]. When the Mo loading reaches 20%, $\text{Al}_2(\text{MoO}_4)_3$, AlVO_4 , and AlVO_7 crystals (JCPDS 46-1687) can be observed (Fig. 1g), indicating that the extra V and Mo species are poorly dispersed on the surface of Al_2O_3 support.

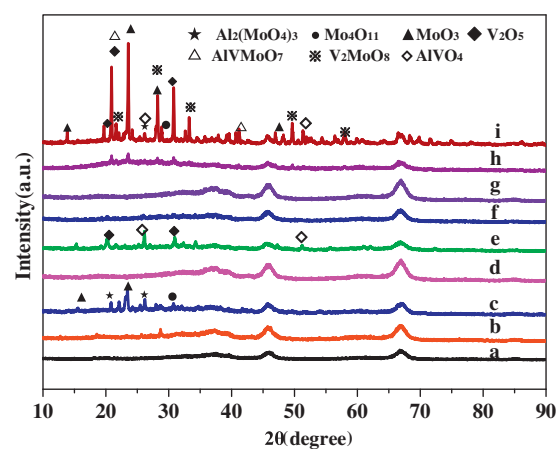


Fig. 1. X-ray diffraction (XRD) patterns of catalysts (a) $\gamma\text{-Al}_2\text{O}_3$, (b) 14 $\text{MoO}_3/\text{Al}_2\text{O}_3$, (c) 24 $\text{MoO}_3/\text{Al}_2\text{O}_3$, (d) 14 $\text{V}_2\text{O}_5/\text{Al}_2\text{O}_3$, (e) 24 $\text{V}_2\text{O}_5/\text{Al}_2\text{O}_3$, (f) 14 $\text{V}_2\text{O}_5\text{-}8\text{MoO}_3/\text{Al}_2\text{O}_3$, (g) 14 $\text{V}_2\text{O}_5\text{-}11\text{MoO}_3/\text{Al}_2\text{O}_3$, (h) 14 $\text{V}_2\text{O}_5\text{-}14\text{MoO}_3/\text{Al}_2\text{O}_3$, and (i) 14 $\text{V}_2\text{O}_5\text{-}20\text{MoO}_3/\text{Al}_2\text{O}_3$.

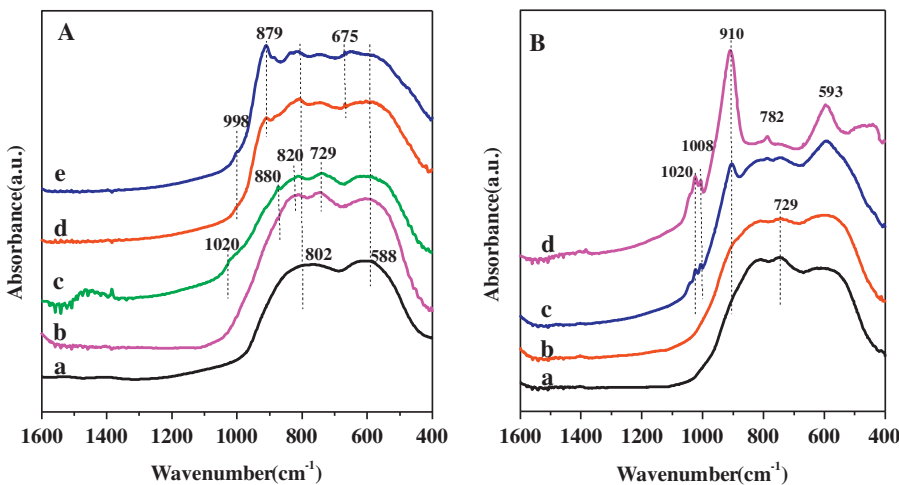


Fig. 2. FTIR spectra of catalysts A: (a) γ -Al₂O₃, (b) 14MoO₃/Al₂O₃, (c) 24MoO₃/Al₂O₃, and (d) 14V₂O₅/Al₂O₃, (e) 24V₂O₅/Al₂O₃; B: (a) 14V₂O₅-8MoO₃/Al₂O₃, (b) 14V₂O₅-11MoO₃/Al₂O₃, (c) 14V₂O₅-14MoO₃/Al₂O₃, and (d) 14V₂O₅-20MoO₃/Al₂O₃.

Structural and vibrational characteristics of molybdenum and vanadium oxides on the Al₂O₃ surface are provided by FTIR spectra of the samples (Fig. 2 and Table 2). The broad bands at 802 and 588 cm⁻¹ originated from δ (OH) vibrations could be the characteristic peaks of the γ -Al₂O₃ framework spectra (Fig. 2A(a)) [3]. For the V₂O₅/Al₂O₃ samples (Fig. 2A(b and c)), the V=O stretches vibration is presented at 1008 and 880 cm⁻¹, while the V—O—V stretching vibration is observed at the band of 820 cm⁻¹. The bands at 1020 cm⁻¹ and 729 cm⁻¹ could be assigned to crystallized V₂O₅ and the V—O—Al vibration of the AlVO₄ crystals, respectively [44–47]. For the MoO₃/Al₂O₃ samples (Fig. 2A(d and e)), the terminal Mo=O stretching vibration of the surface molybdenyl species such as octahedral MoO₆ appears at the band 910 cm⁻¹ and its intensity is enhanced with increasing MoO₃ loadings. The peak at 879 cm⁻¹ could be assigned to the Mo—O—Mo bridge bond stretching vibration of polymolybdates. The weak bands at 675 and 998 cm⁻¹ could be assigned to the MoO₃ crystals and appear at high Mo contents [48–52]. For the 14V₂O₅-xMoO₃/Al₂O₃ catalysts at low MoO₃ loadings (Fig. 2B), the FTIR spectra exhibit no apparent difference compared with the bare Al₂O₃ support (Fig. 2B(a and b)). With the increase of MoO₃ content to 14% (Fig. 2B(c)), the V—O—Mo stretching band at 782 cm⁻¹ is detected [53], confirming the existence of the V₂MoO₈ phase. The new band at 593 cm⁻¹ corresponds to the vibration of Al—O—Mo(V) bonds in the AlO₆ octahedral phase [54], which indicates that extra V and Mo species interact strongly with the Al₂O₃ support, changing the original Al₂O₃ structure of the 14V₂O₅-20MoO₃/Al₂O₃ sample (Fig. 2B(d)), in accordance with XRD results.

To acquire more detailed structural information of V—Mo supported catalysts, Raman spectra for all samples are presented in Fig. 3 and Table 2. The Al₂O₃ support exhibits no absorption

peak (data not shown). For 14V₂O₅/Al₂O₃ (Fig. 3A(a)), there is only a broad band at 750–1000 cm⁻¹ which is assigned to V—O—V stretches in two-dimensional polyvanadates [55]. For 24V₂O₅/Al₂O₃ (Fig. 3A(b)), the band at 1019 cm⁻¹ is assigned to V=O stretches in monovanadates and polyvanadates, and the sharp intense Raman bands at 998, 705, 529, 486, 406, 305, and 289 cm⁻¹ are assigned to crystallized V₂O₅ [56]. 14MoO₃/Al₂O₃ shows bands at 842 cm⁻¹, attributed to Mo—O—Mo stretches of polymolybdates (Fig. 3A(c)). 24MoO₃/Al₂O₃ shows intense bands at 1003, 820 and 380 cm⁻¹, corresponding to crystallized MoO₃. And the band at 1029 cm⁻¹ is attributed to Mo=O stretches (Fig. 3A(d)) [40,57]. For V₂O₅-MoO₃/Al₂O₃ samples in Fig. 3B, the bands at 1003, 771 and 239 cm⁻¹ (corresponding to mixed V—O—Mo phases) is presented in 14V11MoAl, 14V14MoAl and 14V20MoAl, where these characteristic bands are more intense with the increase of Mo content [58,59]. The Mo—V—Al—O mixed oxides also exhibit a Raman band near 1033 cm⁻¹ on the 14V20MoAl sample [40,55]. The Raman analysis is consistent with the FTIR results.

We examine a series of V₂O₅-MoO₃/Al₂O₃ catalysts with a fixed V₂O₅ content of 14% for two reasons: (a) MoO₃ could provide redox sites as well as acidic sites, while V₂O₅ only offers redox sites. By simply adjusting the MoO₃ content, a series of catalysts with different ratio of redox and acidic sites could be prepared. (b) The 14V₂O₅/Al₂O₃ sample is the optimized composition with a considerably high methanol conversion (Table 1), implying that 14% V₂O₅ could provide enough redox sites for methanol oxidation. We also note that high V₂O₅ contents are not favorable for the dispersion of the molybdenum and vanadium on the surface of the support.

3.2. Redox properties

Reducibility of the V₂O₅-MoO₃/Al₂O₃ catalysts and reference samples is characterized by H₂-TPR (Fig. 4). The MoO₃/Al₂O₃ catalysts undergo three stages upon reduction: (1) strongly dispersed monomeric octahedral coordinated Mo and polymolybdates Mo⁶⁺ \rightarrow Mo⁴⁺ (600–750 K), (2) MoO₃ crystal and tetrahedral coordinated Mo⁶⁺ \rightarrow Mo⁴⁺ (750–900 K), and (3) Mo⁴⁺ \rightarrow Mo (900–1200 K) [60]. The H₂ consumption of the 14MoO₃/Al₂O₃ sample shows a first peak at \sim 685 K and a pronounced tailing, which extends up to 1200 K. The 24MoO₃/Al₂O₃ sample presents three wide peaks which could be partially attributed to the reduction of MoO₃ and Al₂(MoO₄)₃ crystals on the catalyst surface [60]. The V₂O₅/Al₂O₃ samples exhibit different behaviors since a single peak is presented near 730–790 K associated with H₂ consumption, which is

Table 2

The IR and Raman band assignments of surface structures for V—Mo/Al catalysts.

Bands	IR Corresponding wavenumber (cm ⁻¹)	Raman corresponding wavenumber (cm ⁻¹)
V=O	1008 and 880	1019
V—O—V	820	750–1000
Mo=O	910	1029, 998
Mo—O—Mo	879	842
V—O—Mo	782	1003, 771 and 239
V—Mo—O—Al	593	1033
V ₂ O ₅	1020	998, 705, 529, 486, 305 and 289
MoO ₃	675 and 998	1003, 820 and 380

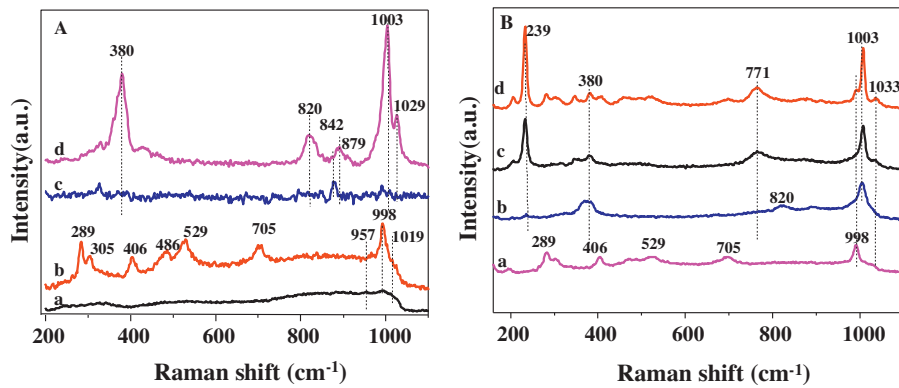


Fig. 3. Raman spectra of catalysts A: (a) $14\text{V}_2\text{O}_5/\text{Al}_2\text{O}_3$, (b) $24\text{V}_2\text{O}_5/\text{Al}_2\text{O}_3$, (c) $14\text{MoO}_3/\text{Al}_2\text{O}_3$ and (d) $24\text{MoO}_3/\text{Al}_2\text{O}_3$; B: (a) $14\text{V}_2\text{O}_5-8\text{MoO}_3/\text{Al}_2\text{O}_3$, (b) $14\text{V}_2\text{O}_5-11\text{MoO}_3/\text{Al}_2\text{O}_3$, (c) $14\text{V}_2\text{O}_5-14\text{MoO}_3/\text{Al}_2\text{O}_3$, and (d) $14\text{V}_2\text{O}_5-20\text{MoO}_3/\text{Al}_2\text{O}_3$.

assigned to reduction of V^{5+} to V^{3+} in various polyvanadates. For the $\text{V}_2\text{O}_5\text{-MoO}_3/\text{Al}_2\text{O}_3$ catalysts, at low MoO_3 contents (Fig. 4e and f), there is only one H_2 consumption peak at the range of 550–900 K, which could be assigned to the overlapped reduction peaks of Mo^{6+} and V^{5+} in $\text{V}-\text{O}-\text{Mo}$ structures to Mo^{4+} and V^{3+} , respectively [55,61]. With the MoO_3 loadings increased to 14%, the temperature of the first peak (T_{\max}) shifts to a lower value, suggesting that the redox ability of catalyst is improved (Fig. 4g). The bulging peak at 789 K could be attributed to the partially reduction of the V_2MoO_8 crystal phases [62,63]. And the peak at 1153 K reflects the reduction of Mo^{4+} to Mo^0 [55]. For the $14\text{V}_2\text{O}_5\text{-}20\text{MoO}_3/\text{Al}_2\text{O}_3$ catalyst (Fig. 4h), T_{\max} of the main H_2 consumption peak shifts back to higher values at around 820 K, which could be due to the appearance of bulk MoO_3 , $\text{Al}_2(\text{MoO}_4)_3$ and AlVMOO_7 that are relatively strongly bonded to the catalyst surface [64].

It is known that the catalytic activity is closely related to the oxygen adsorption capacity and refreshment of lattice oxygen in the catalyst [65]. $\text{O}_2\text{-TPD}$ profiles (Fig. 5) could provide useful information on the behavior of lattice oxygen of composite oxide materials. In the $\text{O}_2\text{-TPD}$ spectra, the first peak of oxygen desorption at 400–500 K is ascribed to the adsorbed oxygen at the surface oxygen sites of the catalyst, while the second peak of oxygen desorption at 600–800 K is attributed to the desorption of a fraction of lattice oxygen on the catalyst surface [66]. The decreasing temperature of the starting point of desorption implies the easier adsorption and activation of gaseous oxygen on the sample. Moreover, the second peak shifts to lower temperatures, indicating the superior

accessibility of the lattice oxygen [67]. The Al_2O_3 support exhibits one single peak at the range of 650–850 K, indicating a weaker gaseous oxygen adsorption ability of the bare Al_2O_3 support compared with V_2O_5 or MoO_3 based samples. The $14\text{V}_2\text{O}_5/\text{Al}_2\text{O}_3$ sample exhibits lower O_2 -adsorption temperature and the second peak is much larger than the $14\text{MoO}_3/\text{Al}_2\text{O}_3$ sample, indicating that V species has stronger oxygen adsorption and activation ability than Mo species. For $\text{V}_2\text{O}_5\text{-MoO}_3/\text{Al}_2\text{O}_3$ samples, it is obvious that the peaks shift to lower temperatures with increasing MoO_3 content, especially for the $14\text{V}_2\text{O}_5\text{-}14\text{MoO}_3/\text{Al}_2\text{O}_3$ sample, demonstrating that $14\text{V}_2\text{O}_5\text{-}14\text{MoO}_3/\text{Al}_2\text{O}_3$ catalyst has stronger adsorption capability for gaseous oxygen and easier migration of lattice oxygen from bulk to surface to complete the oxidation process [68].

To reveal the re-oxidation capability, a series of TPR-TPO tests were carried out. In the re-oxidation profile of the $14\text{V}_2\text{O}_5\text{-}11\text{MoO}_3/\text{Al}_2\text{O}_3$ sample (Fig. 6) that was pre-reduced during TPR, a main peak is observed with a maximum at 610 K, accompanied by a shoulder at lower temperatures. With increasing MoO_3 content in the $\text{V}_2\text{O}_5\text{-MoO}_3/\text{Al}_2\text{O}_3$ catalysts, the main re-oxidation peak progressively shifts from 610 K (for $14\text{V}_2\text{O}_5\text{-}14\text{MoO}_3/\text{Al}_2\text{O}_3$) toward a lower temperature at 540 K, accompanied by a broad peak at 700 K. But for $14\text{V}_2\text{O}_5\text{-}20\text{MoO}_3/\text{Al}_2\text{O}_3$, the peak shifts to higher temperature at 650 K, accompanied by a broad peak at 710 K, which is due to the appearance of crystallized MoO_3 and V_2O_5 . The TPO profiles of the reference samples of $\text{MoO}_3/\text{Al}_2\text{O}_3$ and $\text{V}_2\text{O}_5/\text{Al}_2\text{O}_3$ show a main peak at 650 and 590 K, respectively, indicating that the

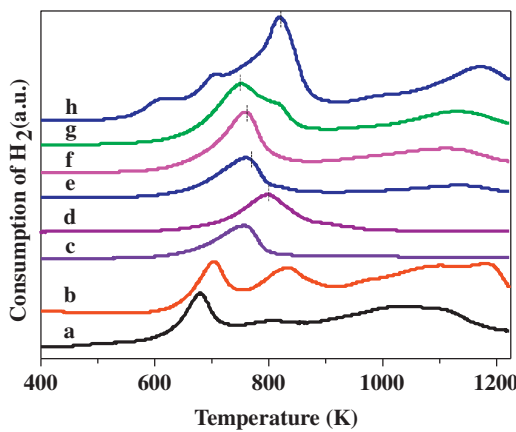


Fig. 4. $\text{H}_2\text{-TPR}$ profiles of catalysts (a) $14\text{MoO}_3/\text{Al}_2\text{O}_3$, (b) $24\text{MoO}_3/\text{Al}_2\text{O}_3$, (c) $14\text{V}_2\text{O}_5/\text{Al}_2\text{O}_3$, (d) $24\text{V}_2\text{O}_5/\text{Al}_2\text{O}_3$, (e) $14\text{V}_2\text{O}_5\text{-}8\text{MoO}_3/\text{Al}_2\text{O}_3$, (f) $14\text{V}_2\text{O}_5\text{-}11\text{MoO}_3/\text{Al}_2\text{O}_3$, (g) $14\text{V}_2\text{O}_5\text{-}14\text{MoO}_3/\text{Al}_2\text{O}_3$, and (h) $14\text{V}_2\text{O}_5\text{-}20\text{MoO}_3/\text{Al}_2\text{O}_3$.

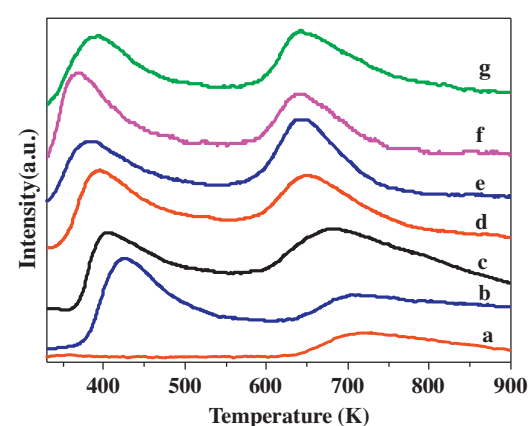


Fig. 5. $\text{O}_2\text{-TPD}$ profiles of catalysts (a) $14\text{MoO}_3/\text{Al}_2\text{O}_3$, (b) $14\text{V}_2\text{O}_5/\text{Al}_2\text{O}_3$, (c) $14\text{V}_2\text{O}_5\text{-}8\text{MoO}_3/\text{Al}_2\text{O}_3$, (d) $14\text{V}_2\text{O}_5\text{-}11\text{MoO}_3/\text{Al}_2\text{O}_3$, (e) $14\text{V}_2\text{O}_5\text{-}14\text{MoO}_3/\text{Al}_2\text{O}_3$, and (f) $14\text{V}_2\text{O}_5\text{-}20\text{MoO}_3/\text{Al}_2\text{O}_3$.

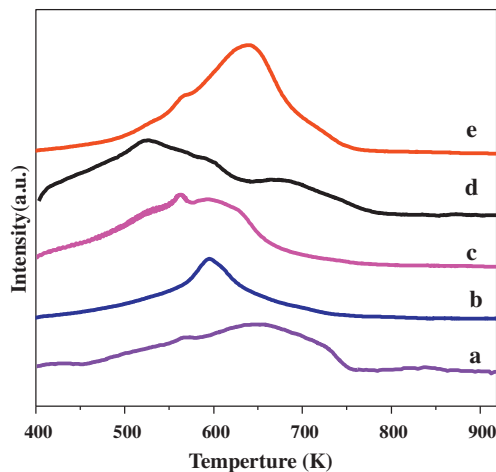


Fig. 6. TPR-TPO profiles of catalysts (a) $14\text{MoO}_3/\text{Al}_2\text{O}_3$, (b) $14\text{V}_2\text{O}_5/\text{Al}_2\text{O}_3$, (c) $14\text{V}_2\text{O}_5\text{--}8\text{MoO}_3/\text{Al}_2\text{O}_3$, (d) $14\text{V}_2\text{O}_5\text{--}11\text{MoO}_3/\text{Al}_2\text{O}_3$, (e) $14\text{V}_2\text{O}_5\text{--}14\text{MoO}_3/\text{Al}_2\text{O}_3$, and (f) $14\text{V}_2\text{O}_5\text{--}20\text{MoO}_3/\text{Al}_2\text{O}_3$.

$\text{V}_2\text{O}_5\text{--MoO}_3/\text{Al}_2\text{O}_3$ sample has stronger re-oxidation ability than the $\text{MoO}_3/\text{Al}_2\text{O}_3$ and $\text{V}_2\text{O}_5/\text{Al}_2\text{O}_3$ samples [69].

The chemical state of V and Mo on the catalyst surface significantly influences the oxidation activity of methanol to DMM, which can be acquired from XPS analysis. Binding energies and peak fitting results of V $2p_{3/2}$ and Mo 3d obtained from XPS spectra of $\text{V}_2\text{O}_5\text{--MoO}_3/\text{Al}_2\text{O}_3$ catalyst are shown in Fig. 7 and Table 3. From the V $2p_{3/2}$ deconvolution results, it is clearly seen that a greater amount of V^{4+} species is presented on the $14\text{V}_2\text{O}_5\text{--}14\text{MoO}_3/\text{Al}_2\text{O}_3$ surface than the $14\text{V}_2\text{O}_5/\text{Al}_2\text{O}_3$ sample, indicating that the degree of reduction of V_2O_5 is enhanced with the MoO_3 addition. For the XPS deconvolution of the molybdenum species, the spin-orbit splitting between the Mo $3d_{5/2}$ and Mo $3d_{3/2}$ signals was fixed to 3.1 eV and the intensity ratio was set to 0.67 [70,71]. When the vanadium substitutes into the $\text{MoO}_3/\text{Al}_2\text{O}_3$, the extent of Mo reduction of $\text{V}_2\text{O}_5\text{--MoO}_3/\text{Al}_2\text{O}_3$ catalysts is also increased significantly. The XPS analysis indicates that the interaction of V and Mo on the catalysts surface would lead to the enhancement of V_2O_5 and MoO_3 reduction [72]. The formation of additional Mo^{5+} and V^{4+} species would contribute to the increased activity. Specifically, the $14\text{V}_2\text{O}_5\text{--}14\text{MoO}_3/\text{Al}_2\text{O}_3$ catalyst possesses much more V^{4+} (17.5%) and Mo^{5+} (12.1%) species than other samples, suggesting that the partially reduced V and Mo species could enhance the activity of

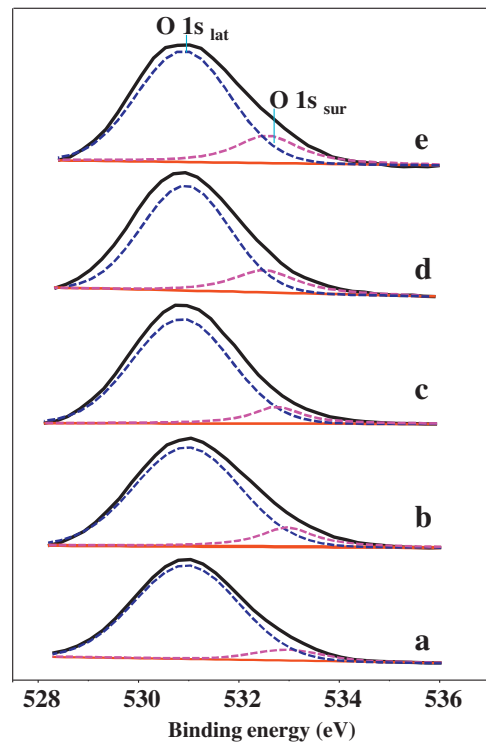


Fig. 8. XPS curve-fitting of O 1s peak of catalysts (a) $14\text{MoO}_3/\text{Al}_2\text{O}_3$, (b) $14\text{V}_2\text{O}_5/\text{Al}_2\text{O}_3$, (c) $14\text{V}_2\text{O}_5\text{--}8\text{MoO}_3/\text{Al}_2\text{O}_3$, (d) $14\text{V}_2\text{O}_5\text{--}14\text{MoO}_3/\text{Al}_2\text{O}_3$, and (e) $14\text{V}_2\text{O}_5\text{--}20\text{MoO}_3/\text{Al}_2\text{O}_3$.

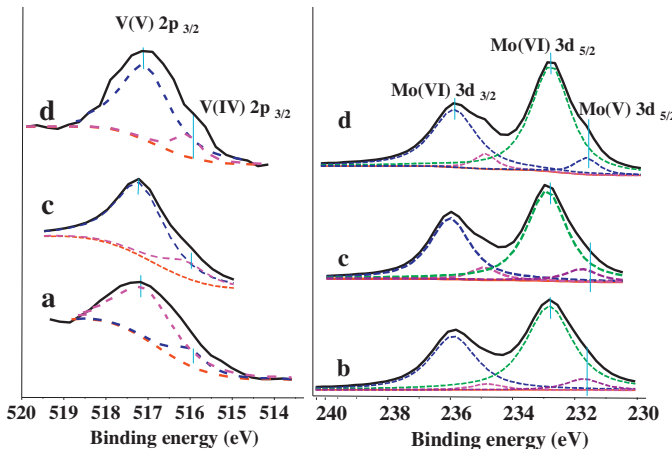


Fig. 7. XPS curve-fitting of V $2p_{3/2}$ and Mo 3d photoelectronic peak of catalysts (a) $14\text{V}_2\text{O}_5/\text{Al}_2\text{O}_3$, (b) $14\text{MoO}_3/\text{Al}_2\text{O}_3$, (c) $14\text{V}_2\text{O}_5\text{--}14\text{MoO}_3/\text{Al}_2\text{O}_3$, and (d) $14\text{V}_2\text{O}_5\text{--}20\text{MoO}_3/\text{Al}_2\text{O}_3$.

methanol oxidation. The enhanced activity might be related to the formation of oxygen vacancies that would improve the adsorption capability of molecular oxygen [73,74].

Additionally, binding energies and peak fitting results of O 1s are shown in Fig. 8 and Table 3. The O 1s peak shows two types of oxygen species. The binding energy at around 530.9 eV is the characteristic of lattice oxygen of Al_2O_3 (531.5 eV), MoO_3 (530.9 eV) and V_2O_5 (529.9 eV), and the binding energy at 532.9 eV can be attributed to active surface oxygen species, including surface oxygen of adsorbed oxygen species, weakly bonded oxygen and hydroxyl-like groups [75–78]. The $14\text{V}_2\text{O}_5/\text{Al}_2\text{O}_3$ has much more active oxygen than $14\text{MoO}_3/\text{Al}_2\text{O}_3$, which might be the most important reason for the higher activity of V species for methanol oxidation. Moreover, the $14\text{V}_2\text{O}_5\text{--}14\text{MoO}_3/\text{Al}_2\text{O}_3$ and $14\text{V}_2\text{O}_5\text{--}20\text{MoO}_3/\text{Al}_2\text{O}_3$ catalysts have higher active oxygen ratio than other V–Mo-based catalysts, resulting in the better performance in methanol oxidation.

3.3. Acidic properties

$\text{NH}_3\text{-TPD}$ profiles of $\text{V}_2\text{O}_5\text{--MoO}_3/\text{Al}_2\text{O}_3$ catalysts with different Mo loadings are shown in Fig. 9. These profiles were deconvoluted with the Gaussian curve fitting method, with results shown in Table 4. The profile of the $\gamma\text{-Al}_2\text{O}_3$ support exhibits the typical peak characteristics of the three well resolved peaks, named as the l, m, and h peaks, which represent weak acidic sites (350–573 K), medium acidic sites (573–693 K) and strong acidic sites (693–873 K), respectively. The strong acidic sites could be observed distinctly on the pure Al_2O_3 support. However, when V_2O_5 or MoO_3 is loaded on the support surface, the strong acidic sites disappear gradually, which implies that the addition of molybdenum or vanadium could cover strong acidic sites. The total acidic sites of the $\text{V}_2\text{O}_5\text{--MoO}_3/\text{Al}_2\text{O}_3$ catalysts tend to increase with the increase of Mo loadings compared with the $14\text{V}_2\text{O}_5/\text{Al}_2\text{O}_3$

Table 3Peak-fitting results of O 1s, V 2p_{3/2} and Mo 3d_{5/2} XPS spectra.

Sample	O1s (eV)		V 2p _{3/2} (eV)		Mo 3d _{5/2} (eV)		V ⁴⁺ /(V ⁴⁺ + V ⁵⁺) (Area %)	Mo ⁵⁺ /(Mo ⁵⁺ + Mo ⁶⁺) (Area %)	O _{sur} /(O _{lat} + O _{sur}) (Area %)
	O _{sur} ^a	O _{lat} ^b	V ⁵⁺	V ⁵⁺	Mo ⁵⁺	Mo ⁶⁺			
14Mo ₃ /Al ₂ O ₃	533.0	531.1	–	–	231.7	232.8	–	6.65	6.7
14V ₂ O ₅ /Al ₂ O ₃	533.0	530.9	515.2	517.1	–	–	3.61	–	12.1
14V ₂ O ₅ –8Mo ₃ /Al ₂ O ₃	532.9	530.9	515.8	517.0	231.5	232.7	6.11	8.95	9.6
14V ₂ O ₅ –14Mo ₃ /Al ₂ O ₃	532.9	530.9	516.1	517.2	231.8	232.9	12.1	17.5	12.8
14V ₂ O ₅ –20Mo ₃ /Al ₂ O ₃	532.8	530.8	516.1	517.1	231.7	232.8	11.2	13.8	14.6

^a O_{sur} = surface active oxygen.^b O_{lat} = lattice oxygen.**Table 4**Acid distribution of V₂O₅–MoO₃/Al₂O₃ catalysts.

Sample	Weak acid (mmol NH ₃ g ⁻¹)	Middle acid (mmol NH ₃ g ⁻¹)	Strong acid (mmol NH ₃ g ⁻¹)	Total (mmol NH ₃ g ⁻¹)	Brønsted sites/Lewis sites
γ-Al ₂ O ₃	7.99	5.40	3.72	17.11	0.00
14Mo ₃ /Al ₂ O ₃	6.76	1.73	2.02	10.51	0.83
14V ₂ O ₅ /Al ₂ O ₃	5.36	2.23	1.09	8.68	0.38
14V ₂ O ₅ –8Mo ₃ /Al ₂ O ₃	7.07	1.46	1.54	10.07	0.50
14V ₂ O ₅ –11Mo ₃ /Al ₂ O ₃	8.95	1.23	1.32	11.50	–
14V ₂ O ₅ –14Mo ₃ /Al ₂ O ₃	11.65	0.71	0.52	12.88	0.98
14V ₂ O ₅ –20Mo ₃ /Al ₂ O ₃	11.19	1.09	0.08	12.36	0.48

catalyst [79]. Meanwhile, an increased amount of weak acidic sites are generated with an increase in Mo content [80].

Fig. 10 shows the FTIR spectra of pyridine adsorption of the catalysts, which is carried out to explore the nature of acidic sites and their effects on the selectivity of DMM. The bands observed at 1450 and 1610 cm⁻¹ are characteristics of Lewis acid sites. The bands at 1540 and 1637 cm⁻¹ are assigned to Brønsted acid sites, whereas the 1490 cm⁻¹ band is related to the coexistence of Brønsted and Lewis acid sites [61]. The Al₂O₃ support only has Lewis acid sites. The presence of the vanadium and molybdenum species on the V₂O₅/Al₂O₃ and Mo₃/Al₂O₃ catalysts could decrease the amount of the Lewis acid sites significantly and produce a trace amount of Brønsted acid sites [48,61]. Spectra for the V₂O₅–MoO₃/Al₂O₃ samples confirm the presence of both Brønsted and Lewis acid sites.

With the increase of Mo loadings, the ratio of Brønsted acid sites to Lewis acid sites rises consequently (Table 4). The partly reduced V and Mo mixed oxides such as Mo⁵⁺ and V⁴⁺ could facilitate the formation of Brønsted acid sites. The enrichment of the Brønsted acid sites could be related to the formation of oxygen vacancy by the reduction of MoO₃ and V₂O₅ [81,82]. We note that when the surface of alumina is populated with small molybdena clusters and molybdoanadates such as V₂MoO₈, the electronegativity of alumina is changed in the vicinity of these molybdena clusters and molybdoanadates, thereby altering the acidic properties [81].

3.4. Catalytic activities

Methanol conversion and selectivity of products on the V₂O₅–MoO₃/Al₂O₃ catalysts are shown in Table 1. The activity of V₂O₅–MoO₃/Al₂O₃ catalysts is significantly higher than that of the corresponding Mo₃/Al₂O₃ and V₂O₅/Al₂O₃ samples. And the 14V₂O₅–14Mo₃/Al₂O₃ sample reaches a maximum conversion rate of 54%. Upon further increase of Mo₃ contents, the conversion decreases slightly. The DMM selectivity of the V₂O₅–MoO₃/Al₂O₃ samples is much higher than the reference

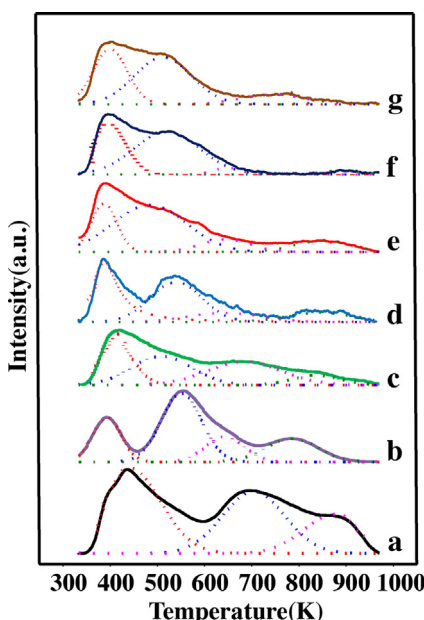


Fig. 9. NH₃-TPD profiles of the catalysts (a) γ-Al₂O₃, (b) 14Mo₃/Al₂O₃, (c) 14V₂O₅/Al₂O₃, (d) 14V₂O₅–8Mo₃/Al₂O₃, (e) 14V₂O₅–11Mo₃/Al₂O₃, (f) 14V₂O₅–14Mo₃/Al₂O₃, and (g) 14V₂O₅–20Mo₃/Al₂O₃.

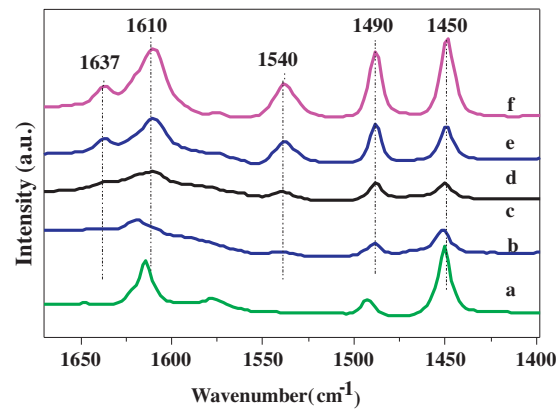


Fig. 10. FTIR spectra of pyridine adsorption on the catalysts (a) γ-Al₂O₃, (b) 14V₂O₅/Al₂O₃, (c) 14Mo₃/Al₂O₃, (d) 14V₂O₅–8Mo₃/Al₂O₃, (e) 14V₂O₅–14Mo₃/Al₂O₃, and (f) 14V₂O₅–20Mo₃/Al₂O₃.

Table 5Catalytic performance at different temperatures for $14V_2O_5$ – $14MoO_3$ /Al₂O₃.

Temperature (K)	Methanol conversion (%)	Selectivity (%)				
		DMM	DME	MF	FA	CO _x
373	36.1	86.4	2.9	10.7	0.0	0.0
393	54.2	92.1	5.6	2.3	0.0	0.0
423	55.5	62.3	10.8	20.8	6.2	0.9
453	57.8	43.4	18.9	26.9	8.7	2.1
473	62.6	11.2	20.3	43.3	14.5	10.7

Feed gas O₂/N₂ = 1/5 vol%; methanol bubbling at 278 K; GHSV = 4000 h⁻¹; reaction time = 8 h.

Mo₃/Al₂O₃ or V₂O₅/Al₂O₃ catalysts. The Mo₃/Al₂O₃ sample has much higher DMM selectivity than V₂O₅/Al₂O₃ with the similar loading. Additionally, the selectivity of other by-products such as DME, MF, FA and CO_x is also given in Table 1. The selectivity of DME decreases with elevated loading of V and Mo species. As Al₂O₃ is favorable for the formation of DME, the covering of acidic sites on Al₂O₃ surface by V–Mo oxides suppresses the DME formation. And the secondary reaction from DME could produce HCHO with the existence of redox sites, which could be subsequently converted to DMM [83]. The increased weak Brønsted acidic sites upon Mo addition could inhibit the formation of oxidation product MF [19].

As temperature has great influence on the activation of reactants, the reactivity of the $14V_2O_5$ – $14MoO_3$ /Al₂O₃ sample is evaluated as a function of temperature and the results are listed in Table 5. The conversion increases with rising temperature. However, the increased conversion is accompanied with a rapid decline in DMM selectivity. When the temperature reaches 393 K, methanol conversion increases significantly to 54.2% and the DMM selectivity reaches a maximum of 92.1%. However, the selectivity of MF and DME increases rapidly with rising temperature. This phenomenon indicates that high reaction temperatures facilitate the formation of MF and DME instead of DMM [1,14]. The formation of FA and CO_x is thermodynamically unfavorable at low temperatures [84]. And the FA and CO_x are not generated until the temperature is raised to 423 K. Since methanol oxidation to DMM is an exothermic reaction, low temperature is favorable for the DMM production. From our results and previous studies [4,20,83,85], one can learn that the product distribution strongly depends on the reaction temperature. Between 343 and 423 K, dimethoxymethane is the major product with a selectivity of 80–95%. The DMM selectivity decreases with rising reaction temperature and the reaction shifts toward methyl formate production. Between 423 and 473 K, methyl formate becomes the main product. The formation of amounts of formaldehyde, formic acid, CO, and CO₂ were observed at a higher temperature of 573 K.

Methanol pulse chemisorption is applied to estimate the amount of active sites and the results are listed in Table 6 (based on Fig. S4). The uptakes of methanol are mainly due to chemisorbed methanol on the active sites because a temperature of 373 K is unlikely to result in physisorbed methanol [86]. With the increase of Mo₃ loadings in $14V_2O_5$ – $xMoO_3$ /Al₂O₃, the uptakes of methanol increase at first and then decrease from 3.84 to 1.16 cm³ g⁻¹. The decrease of methanol uptakes might be caused by the crystallized Mo₃, V₂O₅, Al₂MoO₇ and Al₂(MoO₄)₃ species in $14V_2O_5$ – $20MoO_3$ /Al₂O₃ with poor dispersion of V and Mo species, since the Israel E Wachs has reported the uptakes of methanol chemisorption on bulk crystallized Mo₃, V₂O₅ AlVO₄, Al₂MoO₇ and Al₂(MoO₄)₃ species are much less than the monolayer supported V and Mo species [87–89]. So the poor dispersion of V and Mo species might account for the decrease of methanol uptakes.

The calculation of the activity per site (turnover frequency–TOF) would give insight into the synergistic interaction between the

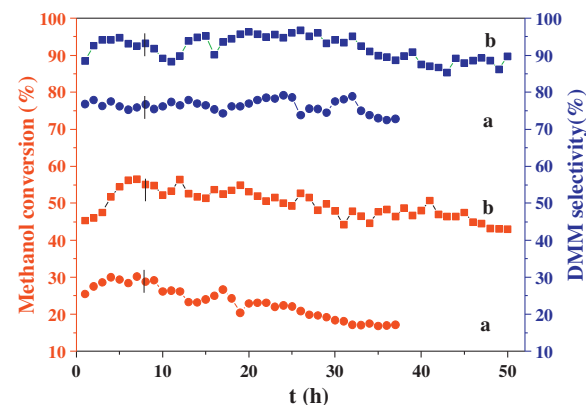


Fig. 11. The long-term reactivity test of the $14MoO_3$ /Al₂O₃ (a) and $14V_2O_5$ – $14MoO_3$ /Al₂O₃ (b) catalysts reacted at 393 K.

V and Mo species during oxidation reactions. Based on methanol chemisorption site densities, the TOF data have been calculated and the results are shown in Table 6 and Fig. S4. It is apparent that $14V_2O_5$ /Al₂O₃ has higher TOF value than $14MoO_3$ /Al₂O₃, which indicates that the V species is more active in methanol oxidation than Mo species. Moreover, the TOF data of the V_2O_5 – MoO_3 /Al₂O₃ catalysts are almost 2–6 times higher than the corresponding V_2O_5 /Al₂O₃ or MoO_3 /Al₂O₃ catalysts, which is owing to the synergistic interaction between the V and Mo species [78].

To investigate the thermal stability of the prepared catalysts, long-term performance tests of $14V_2O_5$ – $14MoO_3$ /Al₂O₃ and $14MoO_3$ /Al₂O₃ were performed at 393 K. Fig. 11 illustrates that the methanol conversion and DMM selectivity of $14V_2O_5$ – $14MoO_3$ /Al₂O₃ sample experience an increase at the first 4 h, then stabilize at around 48% and 90% at the first 40 h test at 393 K, respectively. The $14V_2O_5$ – $14MoO_3$ /Al₂O₃ has a good thermal stability. In comparison, the methanol conversion rate of $14MoO_3$ /Al₂O₃ is much lower than that of $14V_2O_5$ – $14MoO_3$ /Al₂O₃, and undergoes a significant decrease as the reaction proceeds. The activity decreases almost by half after reacting for 36 h. Hence, V addition can increase the thermal stability and catalytic activity, thereby extending the life-time of catalysts.

The thermal stability of the $14V_2O_5$ – $14MoO_3$ /Al₂O₃ and $14MoO_3$ /Al₂O₃ catalysts exhibits a distinct difference, which implies a structural transformation of Mo₃/Al₂O₃ catalyst. The XRD and Raman spectra of the catalysts before and after reaction are shown in Figs. 12 and 13, respectively. The structure of used $14V_2O_5$ – $14MoO_3$ /Al₂O₃ almost remains the original state of the fresh catalyst according to the XRD curves and Raman spectra. However, the used $14MoO_3$ /Al₂O₃ sample presents crystallized Mo₃

Table 6Methanol pulse uptakes on V_2O_5 – (MoO_3) /Al₂O₃ catalysts.

Catalysts	Methanol uptakes (cm ³ g ⁻¹)	N _s ^a = μ mol OCH ₃ m ⁻²	TOF (s ⁻¹) ^b
γ -Al ₂ O ₃	2.07	0.44	0.01
$14MoO_3$ /Al ₂ O ₃	2.27	0.51	0.04
$14V_2O_5$ /Al ₂ O ₃	2.79	0.72	0.05
$14V_2O_5$ – $8MoO_3$ /Al ₂ O ₃	3.57	0.89	0.07
$14V_2O_5$ – $11MoO_3$ /Al ₂ O ₃	3.84	0.96	0.09
$14V_2O_5$ – $14MoO_3$ /Al ₂ O ₃	2.42	0.68	0.17
$14V_2O_5$ – $20MoO_3$ /Al ₂ O ₃	1.16	0.32	0.30

^a Surface active site densities.

^b Turnover frequency based on the methanol conversion and the active sites calculated by the methanol chemisorption. TOF estimation is based on the following equation (X: methanol conversion, F: methanol flow (mL min⁻¹), m: catalyst mass).

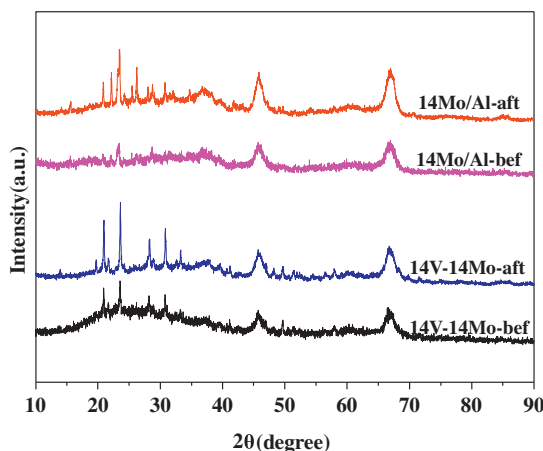


Fig. 12. XRD patterns before and after reaction for $14\text{MoO}_3/\text{Al}_2\text{O}_3$ and $14\text{V}_2\text{O}_5-14\text{MoO}_3/\text{Al}_2\text{O}_3$.

that is not observed in the fresh catalyst as shown in XRD. In Raman spectra, the new bands appear at 1003, 879, 820, and 380 cm^{-1} (corresponding to crystallized MoO_3) for the used $14\text{MoO}_3/\text{Al}_2\text{O}_3$ sample, which is consistent with the XRD result. The molybdenum oxide species tend to aggregate on the catalyst surface and undergo reduction reaction during the methanol oxidation to DMM reaction, leading to the decrease of exposed active Mo species. Even the gaseous oxygen is still available, it could only partially restore the oxidation ability of the catalyst [90]. The consumed Mo species could not be rapidly oxidized into the original state because of its poor re-oxidation ability at low temperatures (TPR after TPO in

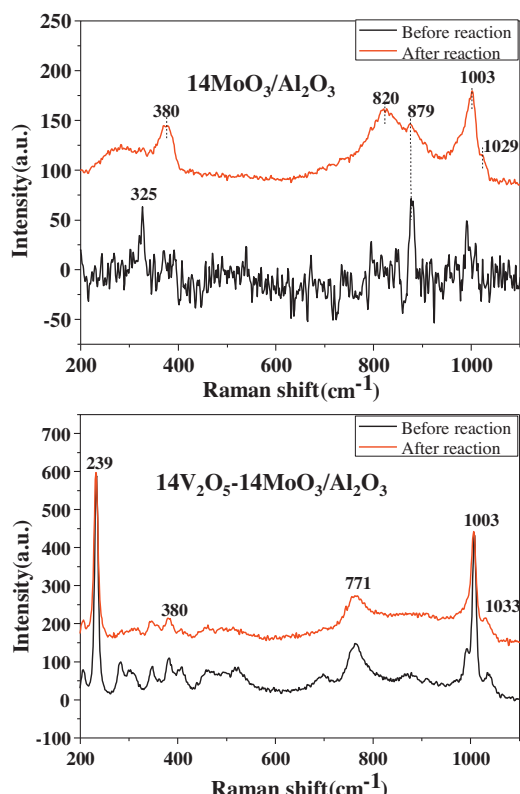


Fig. 13. Raman spectra of the $14\text{MoO}_3/\text{Al}_2\text{O}_3$ and $14\text{V}_2\text{O}_5-14\text{MoO}_3/\text{Al}_2\text{O}_3$ catalysts before and after reaction.

Fig. 6). Meanwhile, the addition of V_2O_5 into the $\text{MoO}_3/\text{Al}_2\text{O}_3$ catalyst could facilitate the dispersion of Mo, inhibiting the aggregation of Mo species and keep the active Mo species at a high concentration for the oxidation reaction.

4. Discussion

4.1. The synergistic effect of vanadium and molybdenum on the methanol oxidation to DMM

The $\text{V}_2\text{O}_5-\text{MoO}_3/\text{Al}_2\text{O}_3$ catalysts exhibit better methanol conversion and DMM selectivity than the reference $\text{MoO}_3/\text{Al}_2\text{O}_3$ and $\text{V}_2\text{O}_5/\text{Al}_2\text{O}_3$ samples, implying the existence of a synergistic effect of V and Mo species. And the synergistic effect of V and Mo species could be further confirmed by the TOF data in Table 6, as the TOF data of $\text{V}_2\text{O}_5-\text{MoO}_3/\text{Al}_2\text{O}_3$ are much higher than the reference samples [78]. We propose that the optimized redox and acidic properties of the V–Mo catalyst are critical to the effectiveness of this synergistic effect, as discussed below. The enhanced redox ability is ascribed to the existence of a redox cycle completed by V–Mo mixed oxides through electron transfer between lattice oxygen and metal cations. The partially reduced V–Mo species introduce an increase amount of oxygen vacancies, which improves the adsorption capability of gaseous oxygen and then the refreshment of lattice oxygen, leading to an enhanced methanol conversion [64,91]. Meanwhile, the weak acidic sites and Brønsted acid sites are ascribed to the addition of MoO_3 and the existence of partially reduced V and Mo species, respectively, which accounts for the increase of DMM yield [2,3,19].

4.2. Active phase

From the structural properties of $\text{V}_2\text{O}_5-\text{MoO}_3/\text{Al}_2\text{O}_3$ catalysts as shown in Figs. 1–3, the interaction between V and Mo is enhanced with the increase of Mo loading, leading to the formation of surface V–O–Mo phase. The V–O–Mo phase is likely to be one of the major active redox phases in the V–Mo based catalysts. It is apparent from Raman spectra (Fig. 10) that the $14\text{V}11\text{MoAl}$, $14\text{V}14\text{MoAl}$ and $14\text{V}20\text{MoAl}$ exhibit plenty of V–O–Mo phases, which results in the enhanced performance on methanol selective oxidation to DMM. Additionally, the reactivities of $24\text{V}_2\text{O}_5/\text{Al}_2\text{O}_3$ and $24\text{MoO}_3/\text{Al}_2\text{O}_3$ catalysts are much lower than the $14\text{V}_2\text{O}_5-11\text{MoO}_3/\text{Al}_2\text{O}_3$ sample, even they have similar loadings of active metal oxides (VO_x together with MoO_x), which further confirms the significant role of the V–O–Mo phase. However, the monovanadates and molybdenyl species bonded to the support could also be the active sites [56,90], since the reactivities and TOF data of $\text{V}_2\text{O}_5/\text{Al}_2\text{O}_3$ and $\text{MoO}_3/\text{Al}_2\text{O}_3$ catalysts are relatively high at appropriate loadings, even not as high as $\text{V}_2\text{O}_5-\text{MoO}_3/\text{Al}_2\text{O}_3$ samples. It is worth noting that neither crystallized V_2O_5 nor MoO_3 is the active phase. First, $24\text{V}_2\text{O}_5/\text{Al}_2\text{O}_3$, $24\text{MoO}_3/\text{Al}_2\text{O}_3$ and $14\text{V}_2\text{O}_5-20\text{MoO}_3/\text{Al}_2\text{O}_3$ present a lot of crystallized V_2O_5 or MoO_3 (Figs. 1–3) and their reactivities (Table 1) are lower than $14\text{V}_2\text{O}_5/\text{Al}_2\text{O}_3$ and $14\text{MoO}_3/\text{Al}_2\text{O}_3$. Furthermore, the used $14\text{MoO}_3/\text{Al}_2\text{O}_3$ catalyst contains a lot of crystallized MoO_3 that causes the deactivation, implying that crystallized MoO_3 is not the active phase.

4.3. Redox cycle

The V–O–Mo oxides, monovanadates and molybdenyl species bonded to support are proposed to be the principal active redox sites in the V–Mo based catalysts, which results in the stronger redox ability. From the H_2 -TPR profiles, the redox ability of $\text{V}_2\text{O}_5-\text{MoO}_3/\text{Al}_2\text{O}_3$ is improved as the T_{\max} shifts to lower values. From the TPR-TPO results, the $\text{V}_2\text{O}_5-\text{MoO}_3/\text{Al}_2\text{O}_3$ has stronger re-oxidation ability than $\text{V}_2\text{O}_5/\text{Al}_2\text{O}_3$ and $\text{MoO}_3/\text{Al}_2\text{O}_3$ catalysts. And

the re-oxidation ability is improved with the increase of MoO_3 content to 14%, which is owing to the accumulation of V–O–Mo phases. Further in-depth analysis (as discussed below) suggests that the enhanced redox ability is attributed to the completion of redox cycle ($\text{Mo}^{5+} + \text{V}^{5+} - \text{Mo}^{6+} + \text{V}^{4+}$) through electron transfer between lattice oxygen and metal cations.

Our hypothesis of the existence of the redox cycle is based on following rationales. According to the Mars–van Krevelen mechanism [74,92], methanol is typically oxidized to FA by the effective lattice oxygen of catalysts, which would be gradually consumed during the reaction process. The low density of effective lattice oxygen causes a decreased activity. Thus, the preservation of high catalytic activity is closely related to the density of effective lattice oxygen, and the recovery of consumed lattice oxygen would be the key step to complete the redox cycle. And the refreshment of lattice oxygen is enabled by the migration of lattice oxygen from bulk to surface which could enhance the adsorption capability of gaseous oxygen [73]. The enhanced migration of lattice oxygen and adsorption of gaseous oxygen could be illustrated by O_2 -TPD, as V_2O_5 – MoO_3 /Al₂O₃ shifts to lower O_2 -adsorption temperatures than V_2O_5 /Al₂O₃ and MoO_3 /Al₂O₃. The formation of oxygen vacancy is realized by the electron transfer between lattice oxygen and metal cations, which is related to the variability of the valence state of V and Mo mixed oxides on the catalyst surface [74,92]. The coexistence of different valence states of V and Mo on V–Mo based catalysts is verified by XPS (Table 3 and Fig. 7). Thus, the electron transfer between lattice oxygen and metal cations plays a critical role in regenerating the catalyst to the original state by restoring the active lattice oxygen. Moreover, the recovery of lattice oxygen is mostly enabled by the V species, since V species exhibit superior performance in the adsorption of gaseous oxygen and stronger re-oxidation ability compared with Mo species, as demonstrated by O_2 -TPD and TPR–TPO. Kaichev has also reported that the presence of gaseous oxygen would lead to a fast re-oxidation of V^{4+} to V^{5+} [92].

The detailed redox cycle is proposed as following [93]. Methanol is adsorbed by donating the electron density from the oxygen atom to surface V^{5+} and Mo^{6+} cations. The adsorbed methanol dissociates to the surface methoxy and hydroxyl groups. Based on previous studies [4,87,92,94–98], we propose that the methoxy groups are coordinated to vanadium and molybdenum cations, whereas hydroxyl groups are formed by the adsorption of hydrogen from $\text{CH}_3\text{O}-\text{H}$ on oxygen atoms bonded to vanadium and molybdenum cations, which results in V–OH and Mo–OH. The surface methoxy groups could be further oxidized to FA by the C–H bond cleavage of the adsorbed methoxy groups, enabled by the consumption of lattice oxygen on the active sites of V and Mo oxides. With the lattice oxygen consumed, the V^{5+} and Mo^{6+} cations are reduced to V^{4+} and Mo^{5+} , accompanied by the formation of oxygen vacancy. Meanwhile, the hydroxyl groups combine with the hydrogen atoms stripped from methoxy species to form water. Furthermore, the reduced V^{4+} and Mo^{5+} could be re-oxidized to their original states by the refreshment of lattice oxygen. It is very likely that the rapid re-oxidation of reduced vanadia occurs via the adsorption of gaseous oxygen at a V(IV) vacancy site to form a peroxide species; one of two oxygen atoms eliminates the V(IV) vacancy, while the other oxygen atom migrates across the V–O–Mo oxide surface until it reaches and eliminates a Mo(V) vacancy. The redox cycle is completed through electron transfer between lattice oxygen and metal cations, which facilitates the perseveration of the high redox capability in methanol oxidation to FA. The generated FA from the redox cycle could further combine two molecules of CH_3OH on favorable acid sites (as discussed in the following section) to produce DMM. Further investigation using in-situ FTIR or Raman is needed in order to explore the specific active sites of V–Mo species in the redox circle.

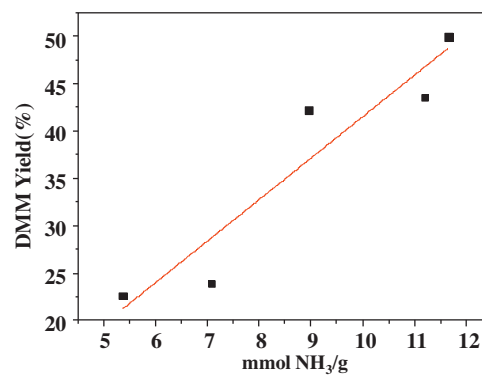


Fig. 14. A correlation between weak acidic sites and the DMM yield of the catalysts.

4.4. The role of weak Brønsted acidic sites

From the NH₃-TPD results shown in Fig. 9 and Table 4, The Al₂O₃ support influences the catalytic performances by providing the necessary acidic sites and helping create a balance for the appreciate acidic and redox sites. It can be seen that the addition of Mo species could produce more weak acidic sites. With the increase of Mo loading, the acidity is decreased since an increasing amount of strong acidic sites are transformed to weak or moderate acidic sites. Moreover, the partially reduced V–Mo mixed oxides result in an increased number of Brønsted acid sites on V_2O_5 – MoO_3 /Al₂O₃ catalysts as shown in the FTIR spectra of pyridine absorption analysis (Fig. 10). The reactivity and distribution of acidic sites (Tables 1 and 4) reveal that the DMM yield is directly proportional to the surface density of the Brønsted acid sites on V_2O_5 – MoO_3 /Al₂O₃ catalysts. The percentage of Brønsted acidic sites on 14V₂O₅–14MoO₃/Al₂O₃ catalyst is at the maximum among all tested samples (Table 4), which accounts for its highest DMM yield among these samples. Moreover, the DMM yield is improved with the increase of weak acid sites upon MoO₃ addition (Fig. 14). Thus, the weak acid sites and Brønsted acid sites are identified as the reason for high DMM yield, in accordance with earlier reports [2,3,19].

4.5. The different role for V and Mo species on methanol conversion and DMM selectivity

Even though vanadium and molybdenum oxides enhance the methanol conversion and DMM selectivity through a synergistic effect, we believe that the two species have played different roles. Confirmed by the conversion and selectivity comparison of the catalysts in Table 1, the vanadium species have a more notable effect on the methanol conversion than Mo species, since V species are more active than Mo species at low temperatures [61]. Moreover, V species could facilitate the dispersion of Mo species and the re-oxidation of reduced molybdena to recover its original state, which could be observed from the comparison of stability performance between 14V₂O₅–14MoO₃/Al₂O₃ and 14MoO₃/Al₂O₃ samples and relative structure characterization (Figs. 11–13). On the other hand, the DMM selectivity for methanol oxidation is significantly influenced by the Mo species. When MoO₃ is added to 14V₂O₅/Al₂O₃ sample, the selectivity of DMM is increased nearly 50% for V_2O_5 – MoO_3 /Al₂O₃ catalysts. The addition of Mo species in V–Mo mixed oxides could generate more weak acidic sites, which is favorable for the increased DMM selectivity.

5. Conclusions

We have described the origin of the reactivity of V_2O_5 – MoO_3 /Al₂O₃ catalysts in methanol selective oxidation to DMM and the roles of molybdenum and vanadium oxides. The V_2O_5 – MoO_3 /Al₂O₃ catalysts have superior performance for DMM production than that of V_2O_5 /Al₂O₃ and MoO_3 /Al₂O₃ reference samples, even at relatively low temperatures. Particularly, the 14 V_2O_5 –14 MoO_3 /Al₂O₃ catalyst exhibits an optimal 54% methanol conversion with a DMM selectivity of 92% at 393 K. The synergistic effect between the surface V and Mo oxide species explains the high catalytic performance for menthol oxidation to DMM. The synergism between V and Mo oxide includes two aspects: (i) The V–O–Mo oxides, monovanadates and molybdenyl species bonded to support are proposed to be the major active redox sites in the V–Mo based catalysts, which results in enhanced redox ability. The V–Mo mixed oxides could complete a redox cycle through the electron transfer between lattice oxygen and metal cations, which improves the redox ability of the catalysts. (ii) The addition of MoO_3 and the existence of partially reduced V–Mo mixed oxides could generate more weak acidic sites and Brønsted acidic sites, which improves the DMM yield. In addition to the synergism between the V and Mo oxide, V species have more notable effects on methanol conversion compared to the Mo species, whereas Mo species have greater influence on DMM selectivity. The importance of the redox cycle and weak acidic sites and Brønsted acidic sites might provide guidance for the future research and design of catalysts.

Acknowledgments

The authors are grateful of financial support by the National Natural Science Foundation of China (21006068, 21222604), the Program for New Century Excellent Talents in University (NCET-10-0611), Specialized Research Fund for the Doctoral Program of Higher Education (20120032110024), the Scientific Research Foundation for the Returned Overseas Chinese Scholars (MoE), and the Program of Introducing Talents of Discipline to Universities (B06006).

Appendix A. Supplementary data

Supplementary material related to this article can be found, in the online version, at <http://dx.doi.org/10.1016/j.apcatb.2014.05.008>.

References

- [1] Y. Zhao, Z. Qin, G. Wang, M. Dong, L. Huang, Z. Wu, W. Fan, J. Wang, *Fuel* 104 (2013) 22–27.
- [2] H. Liu, E. Iglesia, *J. Phys. Chem. B* 107 (2003) 10840–10847.
- [3] S. Chen, Y. Meng, Y. Zhao, X. Ma, J. Gong, *AIChE J.* 59 (2013) 2587–2593.
- [4] H. Zhao, S. Bennici, J. Shen, A. Auroux, *J. Catal.* 272 (2010) 176–189.
- [5] Y. Yuan, Y. Iwasawa, *J. Phys. Chem. B* 106 (2002) 4441–4449.
- [6] Y. Yuan, H. Liu, H. Imoto, T. Shido, Y. Iwasawa, *J. Catal.* 195 (2000) 51–61.
- [7] X. Sécorde, A. Yoboué, E. Berrier, S. Cristol, C. Lancelot, M. Capron, J.-F. Paul, *J. Solid State Chem.* 184 (2011) 2806–2811.
- [8] A. Yoboué, A. Susset, A. Tougerti, D. Gallego, S.V. Ramani, M. Kalyanikar, D.S. Dolzhnikov, S.G. Wubshet, Y. Wang, S. Cristol, *Chem. Commun.* 47 (2011) 4285–4287.
- [9] Y. Yuan, K. Tsai, H. Liu, Y. Iwasawa, *Top. Catal.* 22 (2003) 9–15.
- [10] Y. Yuan, T. Shido, Y. Iwasawa, *Chem. Commun.* (2000) 1421–1422.
- [11] Y.Z. Yuan, H.C. Liu, H. Imoto, T. Shido, Y. Iwasawa, *Chem. Lett.* (2000) 674–675.
- [12] O.A. Nikanova, M. Capron, G. Fang, J. Faye, A.-S. Mamede, L. Jalowiecki-Duhamel, F. Dumeignil, G.A. Seisenbaeva, *J. Catal.* 279 (2011) 310–318.
- [13] L. Briand, R. Bonetto, M. Sanchez, H. Thomas, *Catal. Today* 32 (1996) 205–213.
- [14] X. Lu, Z. Qin, M. Dong, H. Zhu, G. Wang, Y. Zhao, W. Fan, J. Wang, *Fuel* 90 (2011) 1335–1339.
- [15] H. Zhao, S. Bennici, J. Cai, J. Shen, A. Auroux, *Catal. Today* 152 (2010) 70–77.
- [16] H. Guo, D. Li, D. Jiang, H. Xiao, W. Li, Y. Sun, *Catal. Today* 158 (2010) 439–445.
- [17] G. Deo, I.E. Wachs, *J. Catal.* 146 (1994) 323–334.
- [18] H. Guo, Y. CongbiaoChen, J. Xiao, Z. Wang, D. Fan, Y. Li, Sun, *Fuel Process. Technol.* 106 (2013) 77–83.
- [19] S. Chen, S. Wang, X. Ma, J. Gong, *Chem. Commun.* 47 (2011) 9345–9347.
- [20] S. Royer, X. Sécorde, M. Brandhorst, F. Dumeignil, S. Cristol, C. Dujardin, M. Capron, E. Payen, J.-L. Dubois, *Chem. Commun.* 7 (2008) 865–867.
- [21] M. Fournier, A. Aouissi, C. Rocchiccioli-Deltcheff, *J. Chem. Soc., Chem. Commun.* (1994) 307–308.
- [22] S. Damyanova, M.L. Cubeiro, J.L.G. Fierro, *J. Mol. Catal. A: Chem.* 142 (1999) 85–100.
- [23] C. Rocchiccioli-Deltcheff, A. Aouissi, S. Launay, M. Fournier, *J. Mol. Catal. A: Chem.* 114 (1996) 331–342.
- [24] J. Gornay, X. Sécorde, G. Tesquet, B. de Ménorval, S. Cristol, P. Fongaland, M. Capron, L. Duhamel, E. Payen, J.-L. Dubois, *Green Chem.* 12 (2010) 1722–1725.
- [25] K.-a. Thavornprasert, M. Capron, L. Jalowiecki-Duhamel, O. Gardoll, M. Trentesaux, A.-S. Mamede, G. Fang, J. Faye, N. Touati, H. Vezin, *Appl. Catal., B: Environ.* (2013).
- [26] K. Thavornprasert, M. Capron, L. Jalowiecki-Duhamel, O. Gardoll, M. Trentesaux, A.-S. Mamede, G. Fang, J. Faye, N. Touati, H. Vezin, J.-L. Dubois, J.-L. Couturier, F. Dumeignil, *Appl. Catal., B: Environ.* 145 (2014) 126–135.
- [27] M. Nagai, M. Kiyoshi, H. Tominaga, S. Omi, *Chem. Lett.* 29 (2000) 702–703.
- [28] K.S. Seshadri, L. Petrikas, *J. Catal.* 30 (1973) 195–203.
- [29] A. Akbari, M. Omidkhah, J.T. Darian, *World Acad. Sci. Eng. Technol.* 6 (2012) 261–264.
- [30] Y. Li, L. Feng, J. Wang, K. Xu, C. Li, *Acta Petrolei Sin.* 6 (2011) 007 (Petroleum Processing Section).
- [31] J. Gong, X. Ma, S. Wang, X. Yang, G. Wang, S. Wen, *React. Kinet. Catal. Lett.* 83 (2004) 113–120.
- [32] K. Queeney, C. Friend, *J. Phys. Chem. B* 104 (2000) 409–415.
- [33] E.C. Alyea, M.A. Keane, *J. Catal.* 164 (1996) 28–35.
- [34] Y. Matsuoka, M. Niwa, Y. Murakami, *J. Phys. Chem.* 94 (1990) 1477–1482.
- [35] E. Heraclous, M. Machli, A.A. Lemonidou, I.A. Vasalos, *J. Mol. Catal. A: Chem.* 232 (2005) 29–39.
- [36] K. Chen, A.T. Bell, E. Iglesia, *J. Catal.* 209 (2002) 35–42.
- [37] A.P.V. Soares, M.F. Portela, A. Kiennemann, L. Hilaire, *Chem. Eng. Sci.* 58 (2003) 1315–1322.
- [38] Y. Okamoto, F. Morikawa, K. Oh-Hiraki, T. Imanaka, S. Teranishi, *J. Chem. Soc., Chem. Commun.* (1981) 1018–1019.
- [39] W. Kłafkowski, *React. Kinet. Catal. Lett.* 6 (1977) 425–432.
- [40] M.A. Bañares, S.J. Khatib, *Catal. Today* 96 (2004) 251–257.
- [41] O. González-García, L. Cedeño-Caero, *Catal. Today* 150 (2010) 237–243.
- [42] C.C. Yu, S. Ramanathan, F. Sherif, S.T. Oyama, *J. Phys. Chem.* 98 (1994) 13038–13041.
- [43] I.C.L. Leocadio, S. Braun, M. Schmal, *J. Catal.* 223 (2004) 114–121.
- [44] D.E. Keller, T. Visser, F. Soulimani, D.C. Koningsberger, B.M. Weckhuysen, *Vib. Spectrosc.* 43 (2007) 140–151.
- [45] B.M. Reddy, I. Ganesh, E.P. Reddy, *J. Phys. Chem. B* 101 (1997) 1769–1774.
- [46] G. Dąbrowska, P. Tabero, M. Kurzawa, *J. Phase Equilib. Diffus.* 30 (2009) 220–229.
- [47] N. Magg, J.B. Giorgi, T. Schroeder, M. Bäumer, H.-J. Freund, *J. Phys. Chem. B* 106 (2002) 8756–8761.
- [48] I.E. Wachs, *Catal. Today* 27 (1996) 437–455.
- [49] Y. Liu, J. Wang, G. Zhou, M. Xian, Y. Bi, K. Zhen, *React. Kinet. Catal. Lett.* 73 (2001) 199–208.
- [50] L. Lietti, I. Nova, G. Ramis, L. Dall'Acqua, G. Busca, E. Giannello, P. Forzatti, F. Bregani, *J. Catal.* 187 (1999) 419–435.
- [51] K.V.R. Chary, C.P. Kumar, T. Rajiah, C.S. Srikanth, *J. Mol. Catal. A: Chem.* 258 (2006) 313–319.
- [52] Y. Liu, X. Ma, S. Wang, J. Gong, *Appl. Catal., B: Environ.* 77 (2007) 125–134.
- [53] M.O. Guerrero-Pérez, M.C. Herrera, I. Malpartida, M.A. Larrubia, L.J. Alemany, *Catal. Today* 118 (2006) 360–365.
- [54] J. Walczak, P. Tabero, E. Filipek, *Thermochim. Acta* 275 (1996) 249–257.
- [55] S. Yang, E. Iglesia, A.T. Bell, *J. Phys. Chem. B* 109 (2005) 8987–9000.
- [56] T. Kim, I.E. Wachs, *J. Catal.* 255 (2008) 197–205.
- [57] A. Desikan, L. Huang, S. Oyama, *J. Phys. Chem.* 95 (1991) 10050–10056.
- [58] H.-L. Koh, H.-K. Park, *J. Ind. Eng. Chem.* 19 (2013) 73–79.
- [59] R. López-Medina, J. Fierro, M.O. Guerrero-Pérez, M.A. Bañares, *Appl. Catal., A: Gen.* 375 (2010) 55–62.
- [60] T. Malleswara Rao, G. Deo, *AIChE J.* 53 (2007) 1538–1549.
- [61] B. Solsona, A. Dejoz, T. Garcia, P. Concepción, J.M.L. Nieto, M.I. Vázquez, M.T. Navarro, *Catal. Today* 117 (2006) 228–233.
- [62] A. Bielański, M. Najbar, *Appl. Catal., A: Gen.* 157 (1997) 223–261.
- [63] Z. Kang, L. Eyring, *J. Solid State Chem.* 99 (1992) 343–354.
- [64] L. Casagrande, L. Lietti, I. Nova, P. Forzatti, A. Baiker, *Appl. Catal., B: Environ.* 22 (1999) 63–77.
- [65] H. Liu, E. Iglesia, *J. Phys. Chem. B* 109 (2005) 2155–2163.
- [66] A. Yan, B. Liu, Y. Dong, Z. Tian, D. Wang, M. Cheng, *Appl. Catal., B: Environ.* 80 (2008) 24–31.
- [67] W.E. Farneth, F. Ohuchi, R.H. Staley, U. Chowdhry, A.W. Sleight, *J. Phys. Chem.* 89 (1985) 2493–2497.
- [68] J. Zhu, J.G. van Ommen, H.J.M. Bouwmeester, L. Lefferts, *J. Catal.* 233 (2005) 434–441.
- [69] S. Anniballi, F. Cavani, A. Guerrini, B. Panzacchi, F. Trifiro, C. Fumagalli, R. Leanza, G. Mazzoni, *Catal. Today* 78 (2003) 117–129.
- [70] S.J. Khatib, R. Gui-López, M.A. Peña, J.L.G. Fierro, M.A. Bañares, *Catal. Today* 118 (2006) 353–359.

[71] M. Joshi, D. Mukesh, *J. Catal.* 168 (1997) 273–277.

[72] T. Shishido, A. Inoue, T. Konishi, I. Matsuura, K. Takehira, *Catal. Lett.* 68 (2000) 215–221.

[73] L. Jiang, H. Zhu, R. Razzaq, M. Zhu, C. Li, Z. Li, *Int. J. Hydrogen Energy* 37 (2012) 15914–15924.

[74] N. Pernicone, F. Lazzerin, G. Liberti, G. Lanzavecchia, *J. Catal.* 14 (1969) 293–302.

[75] S. Chenakin, R. Prada Silvy, N. Kruse, *J. Phys. Chem. B* 109 (2005) 14611–14618.

[76] X. Huang, J. Liu, J. Chen, Y. Xu, W. Shen, *Catal. Lett.* 108 (2006) 79–86.

[77] W. Xingyi, K. Qian, L. Dao, *Appl. Catal., B: Environ.* 86 (2009) 166–175.

[78] K. Routray, W. Zhou, C.J. Kieley, W. Grünert, I.E. Wachs, *J. Catal.* 275 (2010) 84–98.

[79] M.C. Abello, M.F. Gomez, O. Ferretti, *Appl. Catal., A: Gen.* 207 (2001) 421–431.

[80] K.-I. Segawa, W.K. Hall, *J. Catal.* 77 (1982) 221–231.

[81] W. Suarez, J.A. Dumesic, C.G. Hill Jr., *J. Catal.* 94 (1985) 408–421.

[82] G. Connell, J.A. Dumesic, *J. Catal.* 105 (1987) 285–298.

[83] H. Liu, E. Iglesia, *J. Catal.* 223 (2004) 161–169.

[84] J.N. Allison, W.A. Goddard Iii, *J. Catal.* 92 (1985) 127–135.

[85] Y. Chen, J.L. Fierro, T. Tanaka, I.E. Wachs, *J. Phys. Chem. B* 107 (2003) 5243–5250.

[86] L.E. Briand, W.E. Farneth, I.E. Wachs, *Catal. Today* 62 (2000) 219–229.

[87] L.J. Burcham, L.E. Briand, I.E. Wachs, *Langmuir* 17 (2001) 6175–6184.

[88] I.E. Wachs, K. Routray, *ACS Catal.* 2 (2012) 1235–1246.

[89] L.J. Burcham, L.E. Briand, I.E. Wachs, *Langmuir* 17 (2001) 6164–6174.

[90] M. Brandhorst, S. Cristol, M. Capron, C. Dujardin, H. Vezin, E. Payen, *Catal. Today* 113 (2006) 34–39.

[91] O. Ovsitser, Y. Uchida, G. Mestl, G. Weinberg, A. Blume, J. Jäger, M. Dieterle, H. Hibst, R. Schlögl, *J. Mol. Catal. A: Chem.* 185 (2002) 291–303.

[92] V.V. Kaichev, G.Y. Popova, Y.A. Chesalov, A.A. Saraev, D.Y. Zemlyanov, S.A. Beloshapkin, A. Knop-Gericke, R. Schlögl, T.V. Andrushkevich, V.I. Bukhtiyarov, *J. Catal.* 311 (2014) 59–70.

[93] W.C. Vining, J. Strunk, A.T. Bell, *J. Catal.* 285 (2012) 160–167.

[94] G. Busca, A.S. Elmí, P. Forzatti, *J. Phys. Chem.* 91 (1987) 5263–5269.

[95] V. Ločař, J. Machek, J. Tichý, *Appl. Catal., A: Gen.* 228 (2002) 95–101.

[96] H.Y. Kim, H.M. Lee, R.G.S. Pala, H. Metiu, *J. Phys. Chem. C* 113 (2009) 16083–16093.

[97] J.L. Bronkema, A.T. Bell, *J. Phys. Chem. C* 111 (2007) 420–430.

[98] I.E. Wachs, B.M. Weckhuysen, *Appl. Catal., A: Gen.* 157 (1997) 67–90.